Kent Academic Repository

Full text document (pdf)

Citation for published version

Rivet, Sylvain and Marques, M.J. and Bradu, Adrian and Podoleanu, Adrian G.H. (2017) Passive optical module for polarization-sensitive optical coherence tomography systems. Optics Express, 25 (13). pp. 14533-14544. ISSN 1094-4087.

DOI

https://doi.org/10.1364/OE.25.014533

Link to record in KAR

http://kar.kent.ac.uk/62134/

Document Version

Author's Accepted Manuscript

Passive optical module for polarization-sensitive optical coherence tomography systems

SYLVAIN RIVET,[1,2] MANUEL J. MARQUES,[1,*] ADRIAN BRADU,[1] AND ADRIAN PODOLEANU[1]

[1]*Applied Optics Group, School of Physical Sciences, University of Kent, Canterbury CT2 7NH, UK*
[2]*Laboratoire d'optique et de magnétisme EA938, IBSAM, Université de Bretagne Occidentale, 6 avenue Le Gorgeu, C.S. 93837, 29238 Brest Cedex 3, France*
[*]*M.J.Marques@kent.ac.uk*

Abstract: The paper presents a proof-of-concept polarization-sensitive swept source Optical Coherence Tomography (OCT) system that performs measurements of the retardance as well as of the axis orientation of a linear birefringent sample. The system performs single input state polarization-sensitive OCT and employs an optical module based on optically passive elements such as two beam displacers and a Faraday rotator. Our implementation of the PS-OCT system does not need any calibration step to compensate for the polarimetric effect of the fibers, and its operation does not require a balanced polarization-diversity detector. The optical module allows measurement of the two polarization properties of the sample via two measurements which are performed simultaneously.

References and links

1. M. R. Hee, E. A. Swanson, J. G. Fujimoto, and D. Huang, "Polarization-sensitive low-coherence reflectometer for birefringence characterization and ranging," J. Opt. Soc. Am. B: Opt. Phys. **9**(6), 903–908 (1992).
2. M. K. Al-Qaisi and T. Akkin, "Polarization-sensitive optical coherence tomography based on polarization-maintaining fibers and frequency multiplexing," Opt. Express **16**(17), 13032–13041 (2008).
3. M. Zurauskas and A. G. Podoleanu, "Multiplexing-based polarization sensitive en-face optical coherence tomography," J. Biomed. Opt. **18**(10), 106010–106010 (2013).
4. B. Braaf, K. A. Vermeer, M. de Groot, K. V. Vienola, and J. F. de Boer, "Fiber-based polarization-sensitive OCT of the human retina with correction of system polarization distortions," Biomed. Opt. Express **5**(8), 2736–2758 (2014).
5. Y. Yasuno, S. Makita, T. Endo, M. Itoh, T. Yatagai, M. Takahashi, C. Katada, and M. Mutoh, "Polarization-sensitive complex Fourier domain optical coherence tomography for Jones matrix imaging of biological samples," Appl. Phys. Lett. **85**(15), 3023–3025 (2004).
6. B. Baumann, W. Choi, B. Potsaid, D. Huang, J. S. Duker, and J. G. Fujimoto, "Swept source/Fourier domain polarization sensitive optical coherence tomography with a passive polarization delay unit," Opt. Express **20**(9), 10229–10241 (2012).
7. B. Cense, M. Mujat, T. C. Chen, B. H. Park, and J. F. de Boer, "Polarization-sensitive spectral-domain optical coherence tomography using a single line scan camera," Opt. Express **15**(5), 2421–2431 (2007).
8. M. Pircher, C. K. Hitzenberger, and U. Schmidt-Erfurth, "Polarization sensitive optical coherence tomography in the human eye," Prog. Retin. Eye Res. **30**(6), 431–451 (2011).
9. Y. Yasuno, S. Makita, Y. Sutoh, M. Itoh, and T. Yatagai, "Birefringence imaging of human skin by polarization-sensitive spectral interferometric optical coherence tomography," Opt. Lett. **27**(20), 1803–1805 (2002).
10. S. M. Srinivas, J. F. de Boer, H. Park, K. Keikhanzadeh, L. H. Huai-en, J. Zhang, W. Q. Jung, Z. Chen, and J. S. Nelson, "Determination of burn depth by polarization-sensitive optical coherence tomography," J. Biomed. Opt. **9**(1), 207–212 (2004).
11. W. Trasischker, S. Zotter, T. Torzicky, B. Baumann, R. Haindl, M. Pircher, and C. K. Hitzenberger, "Single input state polarization sensitive swept source optical coherence tomography based on an all single mode fiber interferometer," Biomed. Opt. Express **5**(8), 2798–2809 (2014).
12. N. Lippok, M. Villiger, C. Jun, and B. E. Bouma, "Single input state, single-mode fiber-based polarization-sensitive optical frequency domain imaging by eigenpolarization referencing," Opt. Lett. **40**(9), 2025–2028 (2015).
13. M. Villiger, E. Z. Zhang, S. Nadkarni, W.-Y. Oh, B. E. Bouma, and B. J. Vakoc, "Artifacts in polarization-sensitive optical coherence tomography caused by polarization mode dispersion," Opt. Lett. **38**(6), 923–925 (2013).

14. K. Morishita and K. Yamazaki, "Wavelength and polarization dependences of fused fiber couplers," J. Lightwave Technol. **29**(3), 330–334 (2011).
15. M. Yamanari, S. Makita, and Y. Yasuno, "Polarization-sensitive swept-source optical coherence tomography with continuous source polarization modulation," Opt. Express **16**(8), 5892–5906 (2008).
16. E. Götzinger, B. Baumann, M. Pircher, and C. K. Hitzenberger, "Polarization maintaining fiber based ultra-high resolution spectral domain polarization sensitive optical coherence tomography," Opt. Express **17**(25), 22704–22717 (2009).
17. M. J. Marques, S. Rivet, A. Bradu, and A. Podoleanu, "Polarization-sensitive optical coherence tomography system tolerant to fiber disturbances using a line camera," Opt. Lett. **40**(16), 3858–3861 (2015).
18. J. E. Roth, J. A. Kozak, S. Yazdanfar, A. M. Rollins, and J. A. Izatt, "Simplified method for polarization-sensitive optical coherence tomography," Opt. Lett. **26**(14), 1069–1071 (2001).
19. S. Rivet, M. J. Marques, A. Bradu, and A. Podoleanu, "Optical module to extend any Fourier-domain optical coherence tomography system into a polarisation-sensitive system," J. Opt. **18**(6), 065607 (2016).
20. S. Rivet, M. Maria, A. Bradu, T. Feuchter, L. Leick, and A. Podoleanu, "Complex master slave interferometry," Opt. Express **24**(3), 2885–2904 (2016).
21. A. Bradu, S. Rivet, and A. Podoleanu, "Master/slave interferometry–ideal tool for coherence revival swept source optical coherence tomography," Biomed. Opt. Express **7**(7), 2453–2468 (2016).
22. W. Choi, B. Potsaid, V. Jayaraman, B. Baumann, I. Grulkowski, J. J. Liu, C. D. Lu, A. E. Cable, D. Huang, J. S. Duker, and J. G. Fujimoto, "Phase-sensitive swept-source optical coherence tomography imaging of the human retina with a vertical cavity surface-emitting laser light source," Opt. Lett. **38**(3), 338–340 (2013).
23. M. Villiger, D. Lorenser, R. A. McLaughlin, B. C. Quirk, R. W. Kirk, B. E. Bouma, and D. D. Sampson, "Deep tissue volume imaging of birefringence through fibre-optic needle probes for the delineation of breast tumour," Sci. Rep. **6**, 28771 (2016).
24. S. Makita, M. Yamanari, and Y. Yasuno, "Generalized Jones matrix optical coherence tomography: performance and local birefringence imaging," Opt. Express **18**(2), 854–876 (2010).

1. Introduction

Polarisation-sensitive Optical Coherence Tomography (PS-OCT) methods emerged as early as 1992 [1], evolving from bulk-based to more compact, optical fiber based, designs. PS-OCT systems operating either in time-domain [2, 3] or in frequency-domain [4–7] have been reported for several applications, such as anterior and posterior eye imaging [8], skin imaging [9] and assessment of thermal damage in tissues [10]. To evaluate the retardance and the orientation of the neutral axes of the sample being imaged, at least two polarization measurements must be carried out. They can be performed sequentially or instantaneously, for instance by separating two orthogonal polarization states in a polarization-sensitive beam splitter, or by encoding the measurements in the optical path difference (OPD). However, when single-mode fibers (SMFs) are used in a PS-OCT system, random disturbances in the polarization (due to temperature and mechanical stress) are induced, leading to a bias in the retardance measurement of the sample.

When carrying out polarization measurements, polarization changes induced by SMFs must be controlled by polarization controllers [11] or compensated for via calibration procedures [12].

Usually four polarization measurements are required to obtain the Jones matrix that fully describes the polarization properties of both the fiber and the sample [6]. To peform such measurements, the detector is usually a balanced polarization diversity detector (PDD) and the first surface of the sample is used as a reference to remove the influence of the fibers on the measurement. In fact, most Jones matrix OCT configurations are based on several assumptions: (1) fibers in the sample arm (and all the components in the sample arm such as fiber couplers) do not act as partial polarizers (assumption necessary to avoid projections of polarization states); (2) the first surface of the sample is referred to as an element not exhibiting polarization effects; (3) the polarization mode dispersion (PMD) [13, 14] in fibers is negligible. Moreover, if the balanced PDD is assembled with polarization maintaining (PM) fiber couplers, due to the large birefringence of PM fibers the lengths of the coupler input pigtails should be precisely matched, otherwise additional post-processing would be required [15, 16].

Recently, we reported a novel PS-OCT instrument [17] whose polarization measurements are independent from PMD for a single layer sample structure and that is also insensitive to

any disturbances arising from the couplers. Such a configuration does not use any PDD and its principle of operation is based on two sequential polarization measurements in free space [18]. The set-up employed a specific OCT configuration based on free-space optics in the sample arm. A second set-up [19] was also proposed, which incorporates an optical module in the sample arm of the interferometer that does not require any modification of the interferometer design. This set-up employed a Faraday rotator and two electro-optic polarization modulators, and relied on sequential measurements, requiring additional strategies if the measurement of the axis orientation of the sample was desired.

Here, a novel approach is presented, which overcomes the limitations of the two previously-proposed modules while retaining their advantages. This approach is based on an in-line passive optical module (POM) containing only passive optical elements. This module can be placed in the free space part of the sample arm of any frequency-domain OCT system; in our case, the module was implemented on a swept-source OCT (SS-OCT) system. In addition to the experimental set-up, a theoretical model is presented. The operation of the system is demonstrated on polarization measurements of a Berek waveplate and of a birefringent phantom.

2.   Experimental set-up and principle of operation

In Fig. 1 a schematic diagram of the SS-OCT imaging instrument is presented. It includes, amongst other components, two single-mode fiber couplers (SMC1-2), a polarization controller (PC) in the reference arm of the interferometer, and a balanced photo-detector (BPD). The POM is placed in the sample arm, between the fiber collimator FC1 (producing a collimated beam with a 2 mm diameter) and the galvanometer scanning head SXY, which consists in two galvanometer scanners whose axes are oriented orthogonally to each other. The interface optics in the sample arm also employs a scanning lens SL (Thorlabs, Newton NJ, USA, model LSM03-BB).

The optical source is a tuneable laser (Superlum, Cork, Ireland, model Broadsweeper, with a central wavelength 850 nm, bandwidth 60 nm, line rate 200 Hz). For the detection, a silicon balanced photo-detector with a 10 MHz electronic bandwidth is employed.
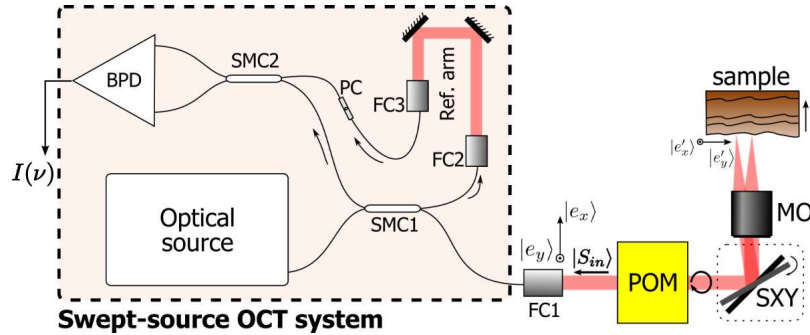

Fig. 1. Swept-source (SS), polarization-sensitive OCT system with the POM installed in the sample arm. The dashed rectangle corresponds to a fiber-based SS-OCT system; POM, passive optical module; SXY, galvanometer scanning head; SL, scanning lens; SMC1-2, single-mode fiber couplers; FC1-3, fiber collimators; PC, fiber-based polarization controller; BPD, balanced photo-detector. All fibers are single mode fibers. $|S_{in}\rangle$ describes the field returning to the fiber-based part of the interferometer. The polarization state is circular after the POM.

The POM has two roles: (i) in the forward direction (from the sample fiber to the sample) it generates a circular polarization state, thus minimising the number of polarization measurements [1], (ii) in the backward direction (from the sample back to the fiber collimator FC1) it analyzes

the polarization state modified by the sample. Since the two roles are performed exclusively in free space, the polarization measurement is insensitive to fiber-induced disturbances, i.e. to birefringence, diattenuation, and to polarization mode dispersion, as experimentally and theoretically demonstrated in [17] and [19]. The POM includes 7 optical components, as depicted in Fig. 2, starting with a linear polarizer (LP) and ending with a quarter-wave plate (QWP), to ensure a circular polarization state of the beam onto the sample (Figure 2). The overall length of the POM is roughly 15 centimeters. The use of a Faraday rotator (FR) and its non-reciprocal behavior enable two functions in the same module: the generation of polarization states, and their analysis. The two beam displacers (BD1 and BD2) together with the dispersion glass (DG) block enable a relative delay of the two orthogonal polarization components of the polarization state modified by the sample. The half-wave plate (HWP) placed between the two BDs ensures that the delay between the two polarization states is only created by the optical length of the DG. In this way, simultaneous measurement of the retardance and of the axis orientation angle becomes possible, as both parameters are encoded on different optical path lengths.

The BDs determine a 4 mm lateral separation between beams, the LP has a contrast above $10^5 : 1$ (Codixx AG), the FR imprints a 22.5º rotation at 850 nm (Leysop Ltd.), and the DG is a 3 mm-thick BK-7 glass block. The QWP and HWP are achromatic waveplates (Thorlabs).

Fig. 2. Passive optical module (POM) processing of waves travelling in (a) the forward direction (from the fiber collimator FC1 to the galvo-scanner SXY) and in (b) the backward direction (from the galvo-scanner SXY to the fiber collimator FC1). LP, linear polarizer oriented at 22.5º according to $|e_y\rangle$; FR, Faraday rotator that induces a 22.5º rotation of the polarization states; BD1 and BD2, beam displacers oriented along $|e_y\rangle$; DG, delay glass block; HWP and QWP, half-wave plate and quarter-wave plate respectively oriented at 45º according to $|e_y\rangle$. The split of paths in each BD is shown with white arrows indicated on their sides. $|e_{back}\rangle$ is the sample polarization state after traversing the quarter-wave plate. $|S_{in}\rangle$ is the polarization state of light returned by the POM from the sample.

In the forward direction, as shown in Fig. 2(a), light is linearly polarized by LP at 22.5º with respect to $|e_y\rangle$ and propagates through the FR which rotates the polarization axis of the linearly polarized light by 22.5º. This aligns the polarization state with the neutral axes of the BDs. The HWP inserted between the two BDs rotates the linear polarization state by 90º, which is subsequently transformed into circular polarization by the QWP. The sample is modelled as a

linear retarder with a net (or double-pass) retardance 2φ, and a fast axis orientation given by θ with respect to the sample basis $\{\,|\,e'_x\rangle,\,|\,e'_y\rangle\,\}$, as defined in Fig. 1. This basis results from the original basis $\{\,|\,e_x\rangle,\,|\,e_y\rangle\,\}$, due to reflections on the two galvanometer scanners of the scanning head SXY, as shown in Fig. 1.

Light back-reflected by the birefringent sample travels through the QWP of the POM. The resulting field $|e_{back}\rangle$ in Fig. 2 (b) has two components on the basis $\{\,|\,e_x\rangle,\,|\,e_y\rangle\}$ as follows:

$$|e_{back}\rangle = \sin\varphi\, e^{2i\theta}\,|e_x\rangle + \cos\varphi\,|e_y\rangle. \tag{1}$$

The range for the one-pass retardance φ is considered from 0 to 90º, while the range for the fast axis orientation θ is measured between -90º and 90º. In the backward direction, each component follows different paths due to the BDs. The $|e_x\rangle$ component follows the same path as in the forward direction while the $|e_y\rangle$ component follows the other displaced path. The HWP, in conjunction with the relative orientation of the BDs, ensures equal optical path lengths for the two orthogonal polarization states in the backward propagation [Fig. 2 (b)]. Considering a thickness of the DG of 3 mm and its approximate index of refraction of 1.5, the optical path delay introduced between the two polarization components by the DG is $\Delta = 1.5$ mm. After the 22.5º rotation imprinted by the FR, both components are oriented at 45º with respect to the LP, and the resulting field $|S_{in}\rangle$ at the input of the probe fiber can be written as:

$$|S_{in}\rangle = \frac{1}{\sqrt{2}}\left(\sin\varphi\, e^{2i\theta} e^{-i\Delta\frac{2\pi}{c}\nu} + \cos\varphi\right)|e_{pol}\rangle, \tag{2}$$

where $|e_{pol}\rangle$ is the linear polarization state selected by the LP, c is the speed of light and ν the optical frequency.

Let us consider a single reflector in the sample arm of the interferometer, placed at position z_0 along the depth coordinate. Due to interference of signals from the reference mirror and from the sample, the spectrum $I(\nu)$ measured by the balanced photo-detector BPD is channeled. The Fourier transform of $I(\nu)$ leads to a A-scan exhibiting two peaks:

$$
\begin{aligned}
\mathfrak{F}\{I(\nu)\} \;=\; & I_{DC} + \frac{1}{\sqrt{2}}\cos\varphi\,(z_0)\,r\,(z_0)\,\mathrm{PSF}\left[\frac{2\,(z-z_0)}{c}\right] \\
& + \frac{1}{\sqrt{2}}\sin\varphi\,(z_0)\,e^{i2\theta(z_0)}r\,(z_0)\,\mathrm{PSF}\left[2\frac{(z-z_0-\Delta/2)}{c}\right] + cc,
\end{aligned} \tag{3}
$$

where cc is the complex conjugate corresponding to the mirror terms and the point-spread function of the system, PSF, is equal to $\mathrm{PSF}(t) = \mathfrak{F}^{-1}\{\langle r_{out}(\nu)|e_{out}(\nu)\rangle\}$.

The complex-valued amplitudes $\hat{A}_1\,(z_0)$ and $\hat{A}_2\,(z_0)$ of the two peaks are related to the polarization properties of the sample as follows:

$$\hat{A}_1\,(z_0) = \frac{1}{\sqrt{2}}\cos\varphi\,(z_0)\,r\,(z_0)\,\mathrm{PSF}(0), \tag{4}$$

$$\hat{A}_2\,(z_0) = \frac{1}{\sqrt{2}}\sin\varphi\,(z_0)\,e^{i2\theta(z_0)}r\,(z_0)\,\mathrm{PSF}(0). \tag{5}$$

At the maximum of the peaks, *i.e.* when the function PSF is evaluated at zero, the inverse FT can be expressed as:

$$\mathrm{PSF}(0) = \int \langle r_{out}(\nu)|e_{out}(\nu)\rangle\,d\nu, \tag{6}$$

which is related to the interference between the reference field $|r_{out}(v)\rangle$ and the sample field $|e_{out}(v)\rangle$ after propagation through the fibers (and the single mode fiber couplers). The sample field $|e_{out}(v)\rangle$ can be written as $|e_{out}(v)\rangle = J_{fiber}(v)\,|e_{pol}\rangle$, where $J_{fiber}(v)$ is the Jones matrix associated with the fibers and couplers. The dependence of J_{fiber} on the optical frequency v describes the PMD of the fibers and couplers. The factor $r(z_0)$ represents the complex-valued reflection coefficient due to a scattering centre located at depth z_0. As shown by Eq. (6), the values of the peak amplitudes $\hat{A}_1(z)$ and $\hat{A}_2(z)$ are related to the projection between $|r_{out}(v)\rangle$ and $|e_{out}(v)\rangle$, impacting the sensitivity of the OCT device. An in-line optical fiber polarization controller (PC) has to be used on the reference arm in order to modify $|r_{out}(v)\rangle$ and maximize the scalar product $\langle r_{out}(v)|e_{out}(v)\rangle$.

The ratio between the moduli of the two peaks determines the one-pass retardance of the sample, $\varphi(z_0)$:

$$\varphi(z_0) = \arctan\left[\left|\frac{\hat{A}_2(z_0)}{\hat{A}_1(z_0)}\right|\right], \tag{7}$$

with $\varphi(z_0) \in [0, 90°]$.

The fast axis orientation angle $\theta(z_0)$ is obtained as:

$$\theta(z_0) = \arg\left[\frac{\hat{A}_2(z_0)}{\hat{A}_1(z_0)}\right]/2 + m\pi, \tag{8}$$

where arg stands for the argument of the complex number $\left(\hat{A}_2(z_0)/\hat{A}_1(z_0)\right)$ and m is an integer such that $\theta(z_0) \in [-90°, 90°]$. As shown by Eqs. (7) and (8), the retardance and axis orientation do not depend on PSF, hence they are both independent of the polarization properties of the fiber. Note that the calculations of $\varphi(z_0)$ and $\theta(z_0)$ originate from the measurement of $\hat{A}_1(z_0)$ and $\hat{A}_2(z_0)$, whose amplitudes depend on the projection between the two fields $\langle r_{out}(v)|e_{out}(v)\rangle$, as stated in the integral in Eq. (6). The PC is adjusted to maximize the product in Eq. (6), knowing that $\left|\hat{A}_1\right|^2 + \left|\hat{A}_2\right|^2 = \frac{1}{2}\left|r(z_0)\,\mathrm{PSF}(0)\right|^2$. The measurement of $\varphi(z_0)$ and $\theta(z_0)$ is more accurate if the peak amplitudes are larger. Moreover, determination of θ when the one-pass retardance φ is 90º is not possible, since the method requires both peaks to be present in the A-scan.

3. Experimental results

Due to the combined effect of the unbalanced dispersion between the two arms of the interferometer and the non-linearity of the swept-source optical frequency tuning, $I(v)$ is chirped. Therefore, a direct Fourier transform of the channeled spectrum $I(v)$ does not provide well-defined peaks $\hat{A}_1$ and $\hat{A}_2$ (as shown by the graphs in Figs. 3 (a) and 3 (b)). Instead of compensating for the dispersion in the reference arm (which would have required a replication of the POM elements in the reference arm) and for the nonlinearity of the tuning, the complex master slave (CMS) processing method is chosen [20, 21] (Figs. 3 (c) and 3 (d)). This consists in generating q digital local oscillators (called masks) and mixing them with the channeled spectra from the sample $I(v)$, where q represents the number of depths of interest. Such a procedure does not require any re-sampling process nor any dispersion compensation. The local oscillators are complex valued and are synthesized from the measurement of a few channeled spectra using a mirror (replacing the sample) placed at different OPD values during a previous calibration step. These masks are chirped due to the unbalanced dispersion in the interferometer and due to the non-linearities associated with the optical frequency tuning of the swept source. For correct POM operation, the two sets of peaks $\hat{A}_1$ and $\hat{A}_2$ are delayed by the DG leading to an unbalanced dispersion which is different for each of the sets. To compensate for the different dispersion seen by the two peaks, which leads to two different PSFs associated to them, different sets of masks are used for each polarization state. To achieve this goal, during the calibration step, the QWP is rotated so that the field $|e_{back}\rangle$ in the backward direction is aligned either along $|e_x\rangle$ or $|e_y\rangle$. The channeled
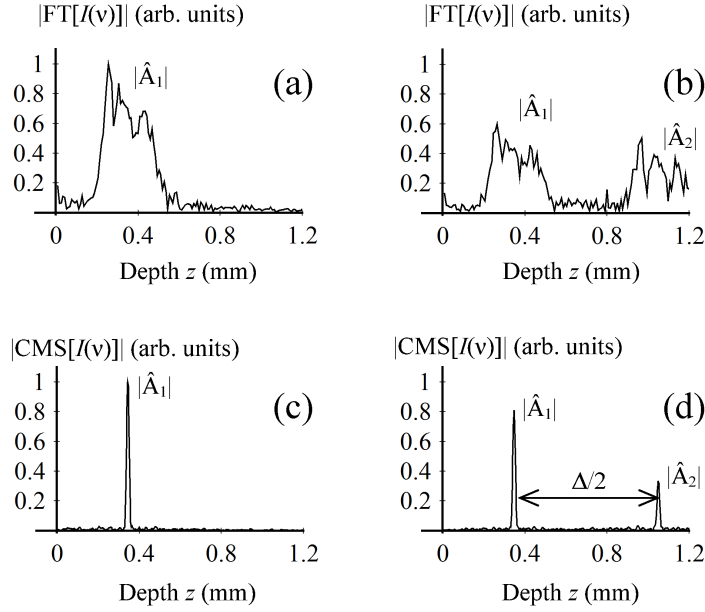
Fig. 3. Comparison of Fourier transform (FT) and complex master slave (CMS) calculations on the channeled spectrum $I(\nu)$ delivered by the BPD unit, for a mirror (respectively (a) and (c)) and for a phantom made from a layer of pressure-sensitive tape coupled to a mirror (respectively (b) and (d)).

spectrum $I(\nu)$ is then mixed with the two sets of masks. The first set of masks leads to the recovery of the amplitude $\hat{A}_1$ and the second set of masks leads to the recovery of the amplitude $\hat{A}_2$, as explained in Fig. 4. Here the cross represents generically a mixer that mixes the masks with the channeled spectrum $I(\nu)$. The mixing process involves a comparison operation that can be accomplished via a dot product, as detailed in Rivet et al. [20].

In Fig. 3, results obtained with two samples are presented: a mirror in Figs. 3(a) and 3(c) and a phantom made by associating a birefringent element (pressure-sensitive tape) and a mirror in 3(b) and 3(d). The Fourier transform of the photo-detected signal is shown in Figs. 3(a) and 3(b) and the CMS operation of the same signal in Figs. 3(c) and 3(d). Due to unbalanced dispersion in the system, the peaks are broad in (a) and (b) while well defined in (c) and (d).

Moreover, due to the variation of sensitivity with depth (drop-off), stemming from the limited coherence length of the swept source, as shown in Fig. 5, a depth-dependent correction is required. The drop-off needs to be measured and compensated for numerically in a calibration step, before performing any calculations involving the two peak signals.

To validate operation of the POM, a comparison of two sets of retardance measurements φ (circles and triangles in Fig. 6) with a calibrated reference is performed. As a calibrated reference, a Berek compensator (Newport, model 5540) and a flat mirror placed in the sample arm are used, between the POM and the galvanometer scanning head SXY. The Berek compensator provides a variable retardance according to its indicator J. Between the two data sets, the Berek compensator is rotated by 45°. For each position of the Berek compensator, 100 measurements are collected in order to evaluate measurement errors (which originate from the settings introduced on the Berek compensator). The measurement errors are associated to systematic errors introduced by the POM adjustments. The standard deviation of the measurements is related to the noise of the detector and the light source. There is a good match between the theoretical prediction and the
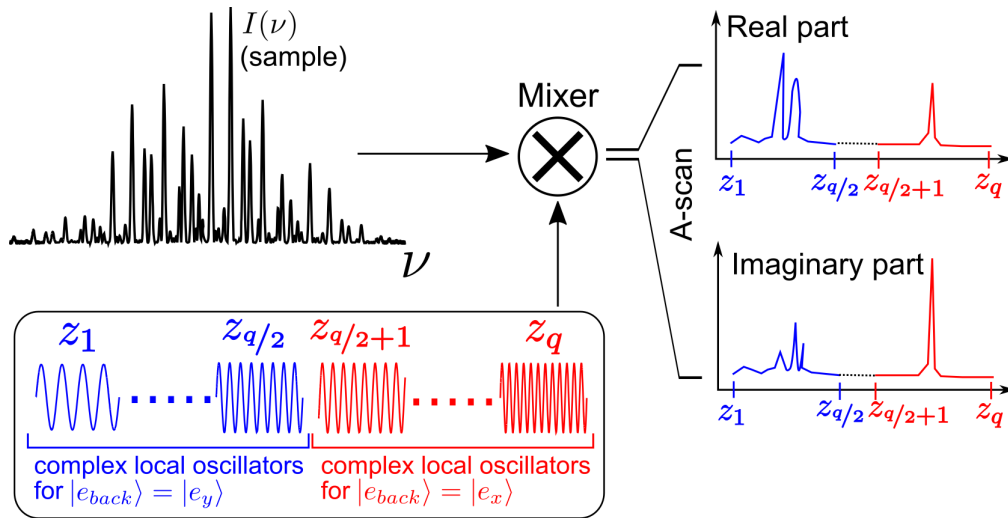
Fig. 4. Schematic representation of the CMS procedure mixing the two sets of digital local oscillators, which correspond to the two orthogonal polarization channels, with the channeled spectra $I(\nu)$ obtained when the sample is imaged.
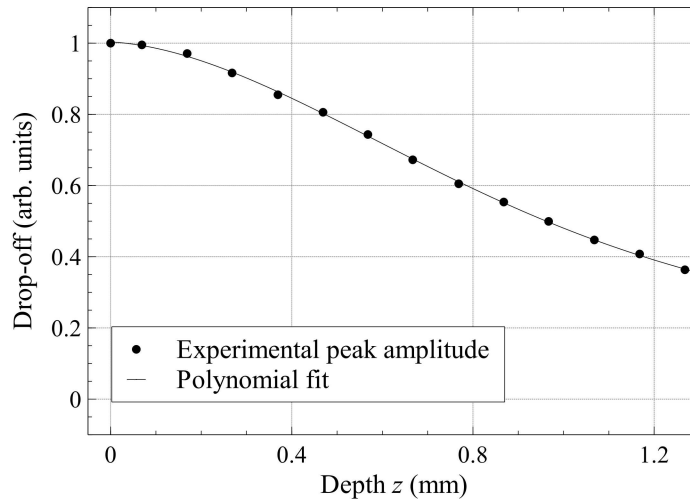

Fig. 5. Experimental drop-off of the peak amplitude versus distance z.

experimental measurements with a maximum bias of $1.5°$ and a standard deviation of less than $0.3°$.

The advantage of using the POM is that there is no need to perform an extra procedure to eliminate the polarization properties of the optical fiber. Such a procedure would have required a $90º$ rotation of the sample around the beam direction. In the case of the Berek compensator this would have been difficult to achieve due to its principle of operation, which involves tilts of the crystal to vary the phase retardance. Advantageously, the POM enables the employment of a thick birefringent structure such as the Berek compensator for the characterization of the PS-OCT operation, as presented in Figs. 6 and 7.
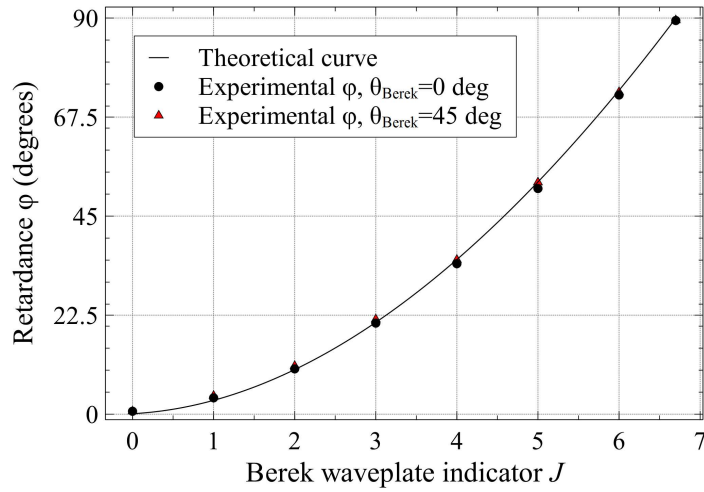
Fig. 6. Measurements of the Berek retardance versus the position of its indicator J. The black line corresponds to the theoretical values of the retardance according to J. Between the two experimental data sets (shown as circles and triangles), the Berek compensator was rotated by 45° around the propagation axis.
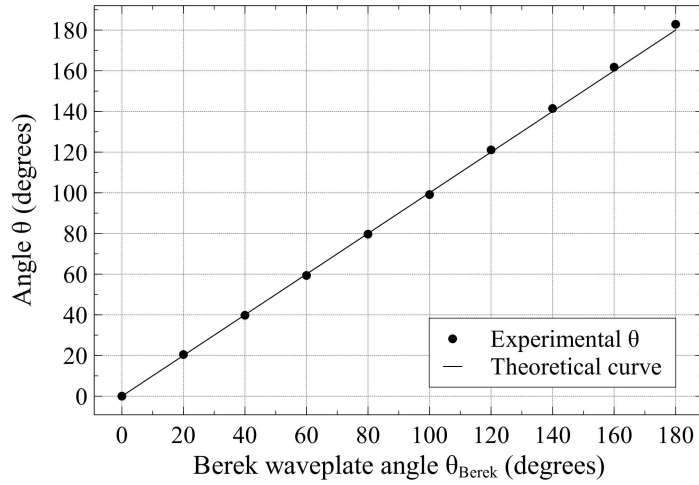

Fig. 7. Measurement of the Berek angle orientation using Eq. (7) (vertical axis) according to the Berek angle orientation θ_{Berek} read on the rotation stage (horizontal axis).

To validate the measurement of the orientation angle of the neutral axis of a sample, the Berek compensator was rotated from $\theta_{\mathrm{Berek}} = 0°$ to $180°$ (Fig. 7) while keeping a fixed retardance roughly equal to 45º. By measuring the phase difference between the peaks $\hat{A}_1$ and $\hat{A}_2$ through Eq. (8), the angle of rotation was measured and compared with the angle read on the rotation stage of the Berek compensator. This was repeated for 100 measurements to determine the deviation of the orientation angle of the neutral axis from the theoretical value and its standard deviation. As the θ angle is known (modulo π), we added π to θ when θ was negative to compare it with the theoretical value θ_{Berek}. There is a good match again between the theoretical

predictions and the experimental measurements with a maximum deviation of 2.8°, as shown by the graph in Fig. 7. Nevertheless, the standard deviation is significant in this case (just under 2.7°), possibly due to the swept-source phase noise. Indeed, SS-OCT is prone to sampling and A-scan trigger jitter, which makes phase-sensitive measurements challenging [22]. To overcome the swept-source phase noise, a new method based on the comparison between adjacent A-scans can be employed [23].

A weak optical power of only $0.78\,\mathrm{mW}$ was achieved at the output of the sample arm fiber, which lowered to $0.64\,\mathrm{mW}$ after the linear polarizer. This was due to several reasons: the polarization state of the light arriving at the fiber collimator FC1 was not completely linearly polarized, low output power from the SS ($\lesssim 3\,\mathrm{mW}$), and a non-optimal splitting ratio in SMC1. The transmission factor γ_{POM} of the POM is $\gamma_{POM} = 0.56$. The value less than 1 is due to losses created by wave reflections at the interfaces of the optical elements used (14 interfaces). After the galvo-scanners and the scan lens (combined transmission 0.69), the incident light power is equal to 0.25 mW. This low power figure combined with similar attenuation for the returning wave makes the imaging of scattering samples difficult.
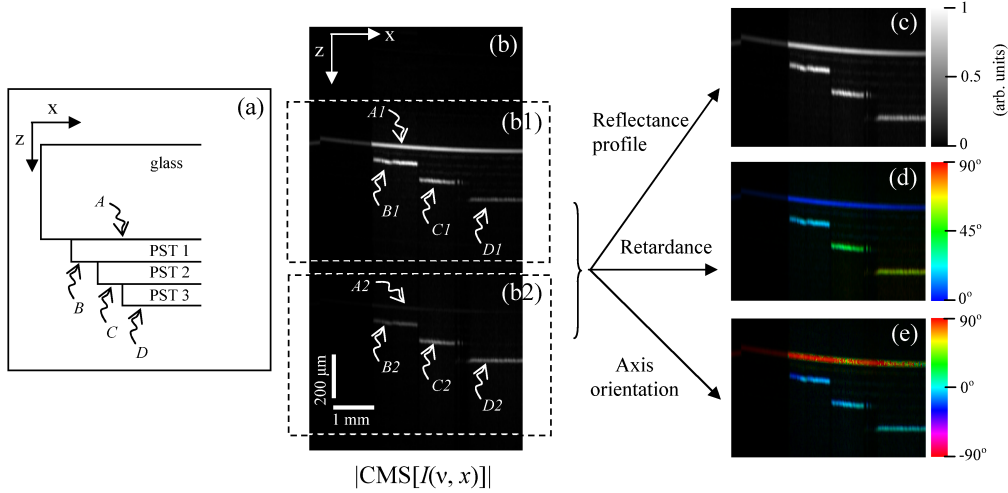

Fig. 8. (a) Sketch of the birefringent sample comprised of a piece of glass on which 3 strips of pressure-sensitive tape (PST) are attached in cascade; (b) B-Scan OCT images inferred using the CMS calculation of the channeled spectra according to the lateral position x, sub-images (b1) and (b2) corresponding to the optical path of the blue and red components in Fig. 2(b) respectively; (c) B-scan of sample retardance; (d) B-scan of the accumulated sample retardance; (e) B-scan of the net axis orientation.

To illustrate the operation of the POM, a phantom made from several specular layers was imaged. This was assembled by using a 1.5 mm piece of anti-reflection coated glass, onto which 3 strips of pressure-sensitive tape (PST, transparent adhesive tape) were laid in cascade, as shown in Fig. 8(a). The PST exhibits linear retardance. The different interfaces within the sample are labelled as A, B, C and D respectively. In Fig. 8(b), a B-Scan (x,z) based on the CMS calculation of the channeled spectra is displayed. The B-scan presents two images (b1) and (b2) of the same sample, corresponding to the optical path travelled by the blue and red polarization components in Fig. 2(b) respectively. For an accummulated retardance below 90º, the larger the sample birefringence, the brighter the sub-image (b2). Due to the optical index matching between the PST layers, there is no back-reflected light from the PST/PST interfaces,

hence only the interfaces PST/air (A) or PST/glass (B–D) can be observed.

Using the sub-images (b1) and (b2), 3 images are produced:

1. Figure 8(c) showing the reflectance profile of the sample obtained as the sum of the amplitude of the sub-images (b1) and (b2).

2. Figure 8(d) showing the accumulated retardance calculated according to Eq. (7).

3. Figure 8(e) showing the axis orientation of the retardance calculated using Eq. (8).

Figures 8(d) and 8(e) are coloured images whose hue depends on the retardance and axis orientation values, and lightness is related to the reflectance profile of Fig. 8(c), with saturation being equal to 1. In Fig. 8(d), the surface A (glass/PST interface) has no retardance, while retardance increases according to the number of PST layers traversed by the laser light. In Fig. 8(e) the axis orientation has been calculated irrespective of the retardance value. However, the values shown for the first interface, corresponding to retardance close to zero in Fig. 8(d), are affected by noise.

Let us consider γ_{POM} as the transmission of the POM calculated through all interfaces apart from the linear polarizer and γ_{input} as the transmission through the linear polarizer in the backward direction. Then, a decrease in the Signal-to-Noise Ratio SNR_{POM} in measuring the reflectivity in Fig. 8(c) using the POM can be evaluated in comparison with the Signal-to-Noise Ratio (SNR) obtained without the POM. Such decrease can be estimated as given by the relation $SNR_{POM} = \left(\gamma_{POM}^2 \gamma_{input}/2\right) SNR$, where the coefficient γ_{input} is related to the extra loss due to the LP preparing a linear state in the forward direction (with $\gamma_{input} = 1/2$ for unpolarized light), and the factor $1/2$ in the bracket is related to the losses stemming from the backward polarization state being oriented at 45º in relation to the axes of the LP. The SNR_{POM} could be improved in multiple ways. The transmission γ_{POM} could be increased by reducing the reflectivity of the anti-reflection coatings. The coefficient γ_{input} could be made closer to 1 by adjusting the polarization in the sample arm or after the light source using suitably placed polarization controllers.

4. Discussion and conclusion

In the PS-OCT configuration presented, a POM is placed at the output of the sample arm fiber collimator FC1. This configuration can provide the retardance and the axis orientation of a birefringent sample. The POM includes passive elements only. By using a circular polarization state towards the sample and performing the analysis in free space, the POM design ensures independence from potential internal disturbances created by optical fibers in the interferometer. Moreover, its operation does not require any measurement based on the first surface of the sample, as demanded by other set-ups, to determine the polarization properties of the fiber. The polarization properties of the sample are instantaneously measured via OPD coding. The in-line design allows the POM to easily be incorporated into any OCT configuration set-up, removing the requirement of polarization diversity detectors which would otherwise be necessary to implement a PS-OCT system.

The single input state PS-OCT can be ambiguous for strong birefringent layered samples. Indeed, if a layer equivalent to a quarter-wave plate transforms the circularly polarized probe beam into a linearly polarized beam and if this linear state is parallel or perpendicular to the neutral axis of the following layer, it is impossible to measure the polarization properties of the second layer. Thus, the retardation measurements of layered sample structures is only possible for weak retardances. In such case, from the measurement of the retardance and the orientation of the optical axis corresponding to a double-pass in depth z, it is straight-forward to construct the corresponding Jones matrix. Then, to achieve the Jones matrix of the local sample structure, the strategy used by Makita *et al.* [24] can be applied.

The POM and the procedure presented can also be extended to spectrometer based OCT instruments within the axial range allowed by the spectrometer. The delay in the POM can proportionally be reduced to accommodate the reduced axial range of spectrometer based OCT instruments, so that thinner objects can be investigated.

Funding